CERN - European Organization for Nuclear Research

LCD-Note-2011-037

Measurement of chargino and neutralino pair production at CLIC

T. Barklow*, A. Münnich†, P. Roloff†

* *SLAC, Stanford, CA 94309, USA*
† *CERN, CH-1211 Geneva 23, Switzerland*

April 23, 2015

Abstract

We present a study performed for the CLIC Conceptual Design Report on the measurement of chargino and neutralino pair production at $\sqrt{s} = 3$ TeV. Fully hadronic final states with four jets and missing transverse energy are considered. Results obtained using full detector simulation and including beam-induced backgrounds for the masses and for the production cross sections of the chargino and the lightest and next-to-lightest neutralinos are discussed.

Contents

1. Introduction **3**

2. Monte Carlo production **3**

3. Event reconstruction **5**

4. Event selection **5**

4.1. Preselection cuts 6

4.2. Event selection using boosted decision trees 6

5. Signal extraction **14**

5.1. Template fit 14

5.2. Least squares method 16

6. Systematic uncertainties **18**

7. Impact of beam polarisation **18**

8. Conclusion and Summary **19**

A. Purities and efficiencies as functions of the $W^{\pm}$ and Higgs energies **20**

B. Details on the least squares fit **20**

1. Introduction

For the CLIC Conceptual Design Report (CDR) [1], several physics processes were selected [2] to benchmark the performance of general purpose detectors at a centre-of-mass energy of 3 TeV. The study presented in this document assumes a SUSY model defined by the mSUGRA parameters $m_{1/2} = 800$ GeV, $A_0 = 0$, $m_0 = 966$ GeV, $\tan\beta = 51$ and $\mu > 0$. In this model, the lightest chargino, $\tilde{\chi}_1^{\pm}$, has a mass of 643.2 GeV, while the masses of the lightest and next-to-lightest neutralinos, $\tilde{\chi}_1^0$ and $\tilde{\chi}_2^0$, are given by 340.3 GeV and 643.1 GeV, respectively. The lightest neutral Higgs boson, h^0, has a mass of 118.5 GeV.

The pair production of charginos and neutralinos is investigated in the following:

$$e^+e^- \to \tilde{\chi}_1^+\tilde{\chi}_1^- \to W^+\tilde{\chi}_1^0 W^-\tilde{\chi}_1^0 \text{ and} \tag{1}$$

$$e^+e^- \to \tilde{\chi}_2^0\tilde{\chi}_2^0 \to h^0(Z^0)\tilde{\chi}_1^0 h^0(Z^0)\tilde{\chi}_1^0, \tag{2}$$

where $BR(\tilde{\chi}_1^{\pm} \to W^{\pm}\tilde{\chi}_1^0) = 100\%$, $BR(\tilde{\chi}_2^0 \to h^0\tilde{\chi}_1^0) = 90.6\%$ and $BR(\tilde{\chi}_2^0 \to Z^0\tilde{\chi}_1^0) = 9.4\%$. Hadronic decays of the $W^{\pm}$, h^0 and Z^0 bosons are considered and hence the investigated final state signature is given by four quarks and missing transverse energy. The reconstruction of chargino and neutralino pair production allows to benchmark the reconstruction of hadronically decaying gauge bosons in multi-hadron final states.

2. Monte Carlo production

The physics events used for the study presented here were generated using the WHIZARD 1.95 [3] program. Initial and final state radiation (ISR and FSR) were enabled during the event generation. The treatment of ISR in WHIZARD is based on the LLA structure function [4]. The luminosity spectrum expected at CLIC was used during the event generation [5]. The hadronisation of final state partons was simulated using PYTHIA [6]. The CLIC_SiD_CDR [7] detector geometry model was used. The generated events were passed through the detector simulation program SLIC [8] which is based on the Geant4 [9] package.

The centre-of-mass energies of the hard interactions for chargino and neutralino pair production events, $\sqrt{s'}$, for the CLIC luminosity spectrum and after ISR are shown in Fig. 1. The distributions have long tails down to the pair production thresholds.

Events were overlayed with pileup from $\gamma\gamma \to$ hadrons interactions corresponding to 60 bunch crossings [10]. The reconstruction chain included an improved version [11] of the PandoraPFA [12] algorithm to reconstruct particle flow objects.

An overview of all produced Monte Carlo (MC) samples is given in Tab. 1. Dedicated samples for the considered signals corresponding to large luminosities are available. Additionally, backgrounds from SUSY and Standard Model (SM) processes were used in the study presented in this note.

As a cross check, additional event samples for the production of W^+W^- and Z^0Z^0 pairs generated using PYTHIA were used. The cross sections for events where $\sqrt{s'}$ is larger than 1.6 TeV are 728 fb^{-1} and 54 fb^{-1}, respectively[1)]. However, the changes of the results shown

[1]The cut of 1.6 TeV was imposed since the PYTHIA samples were originally generated for another study. It is expected that the conclusions given in this note are not affected by this cut.

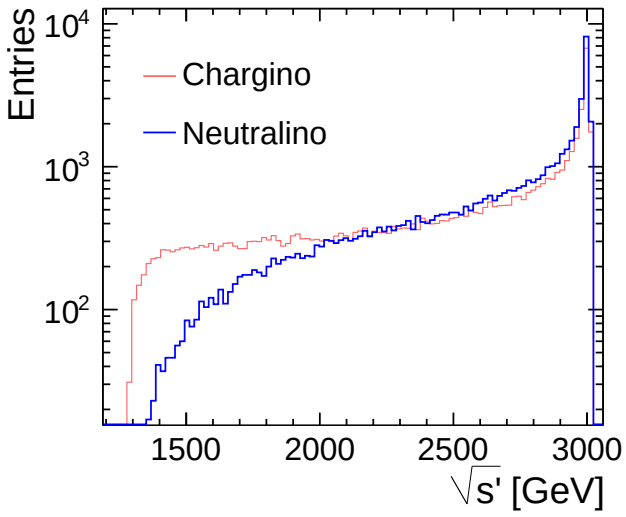

Figure 1: Distribution of the centre-of-mass energies of the hard interactions for chargino (red) and neutralino (blue) pair production events. The distributions extend down to the pair production thresholds.

Type	Process	Cross section [fb]	Luminosity [ab^{-1}]	Referenced with
Signal	$\tilde{\chi}_1^+\tilde{\chi}_1^-$	10.6	13.4	Chargino
	$\tilde{\chi}_2^0\tilde{\chi}_2^0$	3.3	23.8	Neutralino
Background	$\tilde{\chi}_2^+\tilde{\chi}_2^-$	10.5	1.8	SUSY
	$\tilde{\chi}_1^+\tilde{\chi}_2^-$	0.8	8.9	
	$\tilde{\chi}_1^+\tilde{\chi}_1^-\nu\overline{\nu}$	1.4	21.9	
	$\tilde{\chi}_2^0\tilde{\chi}_2^0\nu\overline{\nu}$	1.2	13.3	
	$q\bar{q}q\bar{q}\nu\overline{\nu}$	95.4	4.5	SM
	$q\bar{q}h^0\nu\overline{\nu}$	3.1	6.2	
	$h^0h^0\nu\overline{\nu}$	0.6	22.8	

Table 1: Cross sections and integrated luminosities of the available Monte Carlo samples for chargino and neutralino pair production and for SUSY and Standard Model backgrounds. The charge conjugated modes are implied throughout this document.

in this document are negligible when the W^+W^- and Z^0Z^0 events are included. Hence these final states are excluded from the analysis presented in the following except explicitly stated otherwise.

3. Event reconstruction

The steps to reconstruct events with four jets from particle flow objects (PFOs) are described in this section. The presence of pileup from the process $\gamma\gamma \to$ hadrons increases the number of reconstructed PFOs in typical signal events by a factor 10 and the total visible momentum by a factor four within the readout time window of the detector. On the other hand, the background particles are emitted mostly in the forward direction.

A large fraction of the background can be rejected using combined timing and transverse momentum cuts. The effects of different variants of these timing cuts referred to as "loose selected PFOs", "selected PFOs" and "tight selected PFOs" are illustrated in Fig. 2. In the following, the "tight selected PFOs" are used unless explicitly stated otherwise.

Only events containing at least four reconstructed PFOs with $p_T > 250$ MeV were used further. Events with at least one identified electron or muon with $p_T > 20$ GeV were rejected.

Jets were reconstructed from PFOs using the k_t algorithm [13] as implemented in FastJet [14] in its exclusive mode with R = 0.7 and using the E recombination scheme. The clustering was stopped when four jets were found. To reject leptonic decays of $W^{\pm}$, Z^0 or Higgs bosons further, all jets were required to contain more than one PFO.

Bosons candidates were formed from jet pairs minimising:

$$(M_{jj,1} - M_{W^{\pm},h^0})^2 + (M_{jj,2} - M_{W^{\pm},h^0})^2, \tag{3}$$

where $M_{jj,1}$ and $M_{jj,2}$ are the masses of the two reconstructed jet pairs and $M_{W^{\pm},h^0}$ was set to the world average of the $W^{\pm}$ boson mass to reconstruct $\tilde{\chi}_1^{\pm}$ and to the assumed Higgs boson mass to reconstruct $\tilde{\chi}_2^0$.

The reconstruction of $W^{\pm}$ bosons in $\tilde{\chi}_1^+\tilde{\chi}_1^-$ events is illustrated in Fig. 3. The distributions obtained with and without the overlay of $\gamma\gamma \to$ hadrons are compared. A good reconstruction of $W^{\pm}$ bosons was achieved if tight timing cuts were applied to select the PFOs used as input to the jet reconstruction. The right plot in Fig. 3 shows the reconstructed masses for the two selected signal data sets: chargino pairs decaying into W^+W^- and neutralino pairs decaying into either h^0h^0 or h^0Z^0. The event samples were scaled to have similar number of events for each channel. Since less than 1% of the neutralino pairs decay to the Z^0Z^0 final state, this contribution is not shown in the figure. The horizontal band for $M_{jj,2} \approx M_{h^0}$ and $M_{jj,1} < M_{h^0}$ is caused by $\tilde{\chi}_2^0\tilde{\chi}_2^0 \to h^0\tilde{\chi}_1^0h^0\tilde{\chi}_1^0$ events where one of the h^0 bosons is only partially reconstructed. No similar vertical band is visible due to the way the jets are ordered in the analysis.

4. Event selection

The selection of $\tilde{\chi}_1^+\tilde{\chi}_1^-$ and $\tilde{\chi}_2^0\tilde{\chi}_2^0$ pair production events is performed in two steps. First, a cut-based preselection is applied. The remaining background events are suppressed further using boosted decision trees in a second step. These two steps are described in the following two subsections.

4.1. Preselection cuts

To restrict the training of the boosted decision trees to the region where the signal purities are high, the following preselection cuts are applied:

- $40 < M_{\mathrm{jj},1} < 160\,\mathrm{GeV}$ and $40 < M_{\mathrm{jj},2} < 160\,\mathrm{GeV}$
- $|\cos\theta^{\mathrm{miss}}| < 0.95$, where θ^{miss} is the polar angle of the missing momentum
- Angle between the $W^{\pm}$ or Higgs candidates larger than 1 radian
- $|\cos\theta^{\mathrm{jj},1}| < 0.95$ and $|\cos\theta^{\mathrm{jj},2}| < 0.95$, where $\theta^{\mathrm{jj},1}$ and $\theta^{\mathrm{jj},2}$ are the polar angles of the two jet pairs

The same preselection cuts were used for the selections of chargino and neutralino pair production. 55% of the chargino signal events and 27% of the background events pass the preselection cuts. For the neutralino, 62% of the signal events and 26% of the background events are accepted by the preselection.

4.2. Event selection using boosted decision trees

To distinguish between signal and background events further, the Toolkit for Multivariate Analysis (TMVA) [15] was used. Boosted decision trees proved to be the most efficient classifiers for this analysis. For training purposes, 20% of the available events for each process were used. These events were not considered in the analysis to measure masses or cross sections.

Event classification

The boosted decision trees were trained using 15 variables describing the event topology and describing kinematic quantities of the reconstructed $W^{\pm}$ or Higgs candidates:

- Missing transverse momentum
- Thrust of the event
- Oblateness of the event
- Sum of the transverse energies of both $W^{\pm}$ or Higgs candidates
- $\cos\theta^{\mathrm{jj},1}$ and $\cos\theta^{\mathrm{jj},2}$ as defined in Sec. 4.1
- Invariant masses, $M_{\mathrm{jj},1}$ and $M_{\mathrm{jj},2}$, of each $W^{\pm}$ or Higgs candidate, and of the sum of both
- Angle between the two $W^{\pm}$ or Higgs candidates
- θ^{miss} as defined in Sec. 4.1
- Weighted charge of each jet pair, $\frac{\sum_i q_i \cdot (p_i^{\mathrm{PFO}})^{\kappa}}{\sum_i (p_i^{\mathrm{PFO}})^{\kappa}}$, where the sum runs over all all PFOs, p_i^{PFO} is the momentum of the i^{th} PFO and $\kappa = 1.8$

- Number of reconstructed particles in each jet pair

As examples for the input variables, the invariant masses and polar angles of the $W^{\pm}$ candidates for the chargino signal and the SM and SUSY backgrounds are shown in Fig. 4. The signal candidates are more central than the SM background and show a sharp peak at the nominal $W^{\pm}$ mass.

Two separate boosted decision trees were trained, one considering chargino pair production as signal and the other one considering neutralino pair production as signal. All other MC samples were treated as background.

Using the input variables described above, the classifier response for each event was computed which is referred to as BDT in the following. Figure 5 shows the distribution of the BDT for the chargino signal and for the SM and SUSY backgrounds. Signal events tend to higher BDT values than the backgrounds. Additionally, the signal efficiency and purity for events passing the preselection as a function of the chosen BDT cut value are shown.

Figure 6 shows the same histograms for the neutralino as signal. The event selection classifiers for both signals show similar performance. For large BDT values, the SM background has the largest overlap with the signal for the chargino while SUSY processes represent the dominant background for the neutralino signal. The same cut of BDT > 0.05 was used in both cases.

The efficiencies of the entire selection chain consisting of the preselection and of the BDT cut for reconstructed chargino and neutralino signal events are 25% and 33%, respectively. The signal purities in the selected samples are 57% for the chargino and 55% for the neutralino.

Additionally, the efficiencies and purities for the chargino and neutralino selections as a function of the $W^{\pm}$ or Higgs candidate energies for different BDT cuts are shown in Appendix A.

Properties of selected events

In the following, properties of the chargino and neutralino selections using boosted decision trees and of the selected events are described. The signals and all backgrounds were scaled to an integrated luminosity of 2 ab^{-1}.

The energies of the reconstructed $W^{\pm}$ candidates before and after the chargino selection are shown in Fig. 7. The plots demonstrate the significant improvement of the signal-to-background ratio due to the event selection. The corresponding histograms for the invariant masses are shown in Fig. 8.

The energies of the reconstructed Higgs candidates before and after the neutralino selection are shown in Fig. 9. The same histograms for the masses of the Higgs candidates are shown in Fig. 10. Apart from the large peak caused by the dominant decay of the $\tilde{\chi}_2^0$ to a Higgs, a small contribution from decays into Z^0 bosons is visible.

Finally, the different contributions to the SUSY background passing the chargino and neutralino selections are shown in 11. The contribution from the neutralino pair production to the chargino signal are very small and vice versa.

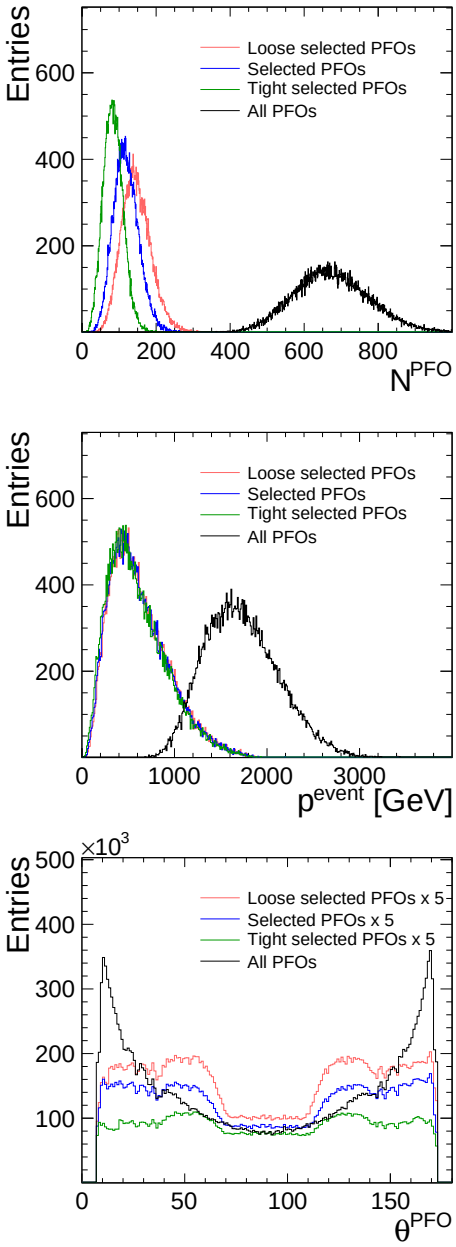

Figure 2: Number of reconstructed PFOs per event (top), momentum of all PFOs per event (middle) and inclination of all PFOs (bottom) in chargino signal events. Different variants of the combined timing and momentum cuts to remove pileup from beam-induced backgrounds are compared to the distributions obtained without selection cuts.

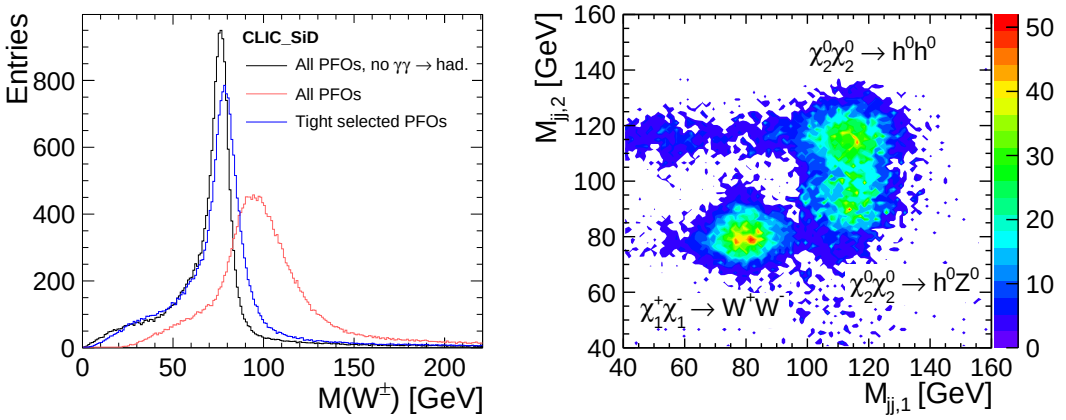

Figure 3: Reconstructed mass of $W^{\pm}$ candidates without and with pileup from $\gamma\gamma \to$ hadrons. For events with pileup, the distribution for all PFOs is compared to that obtained using combined timing and momentum cuts (left). 2D mass plot of the signal final states for different decays of chargino and neutralino pairs with pileup (right).

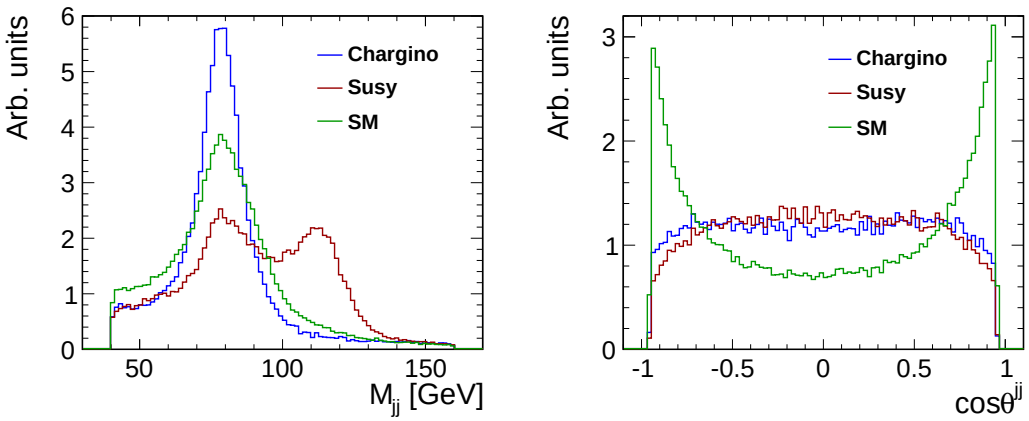

Figure 4: Invariant masses (left) and polar angles (right) of the $W^{\pm}$ candidates for the chargino signal and the SM and SUSY backgrounds. The normalisation of all distributions is arbitrary to illustrate the different shapes.

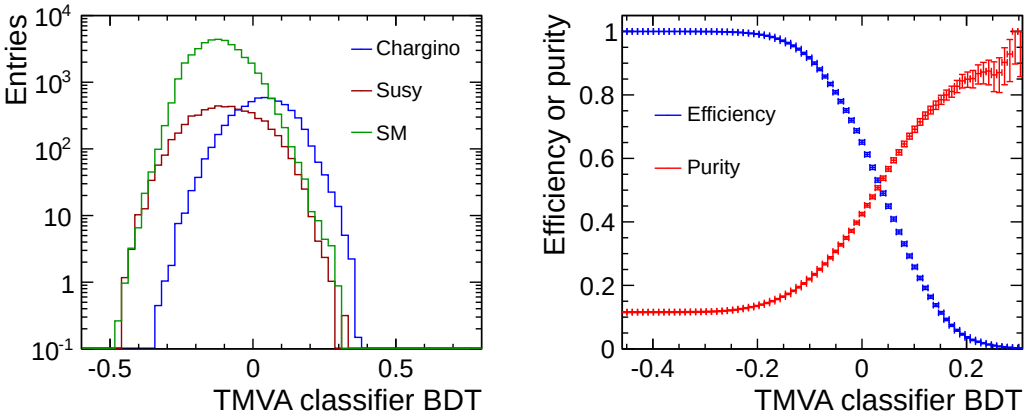

Figure 5: Distribution of the BDT values for the chargino signal and its background for 2ab^{-1} (left) and the selection efficiency and purity in dependence on the chosen BDT cut value (right).

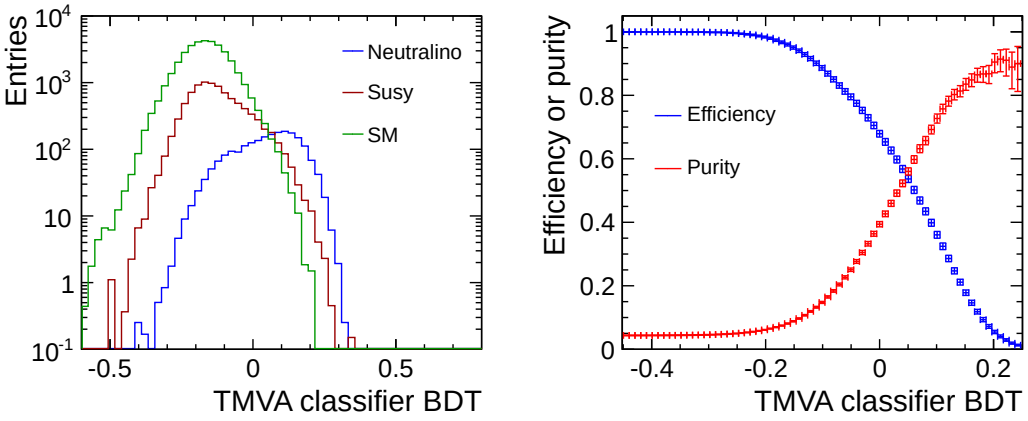

Figure 6: Distribution of the BDT values for the neutralino signal and its background for 2ab^{-1} (left) and the selection efficiency and purity in dependence on the chosen BDT cut value (right).

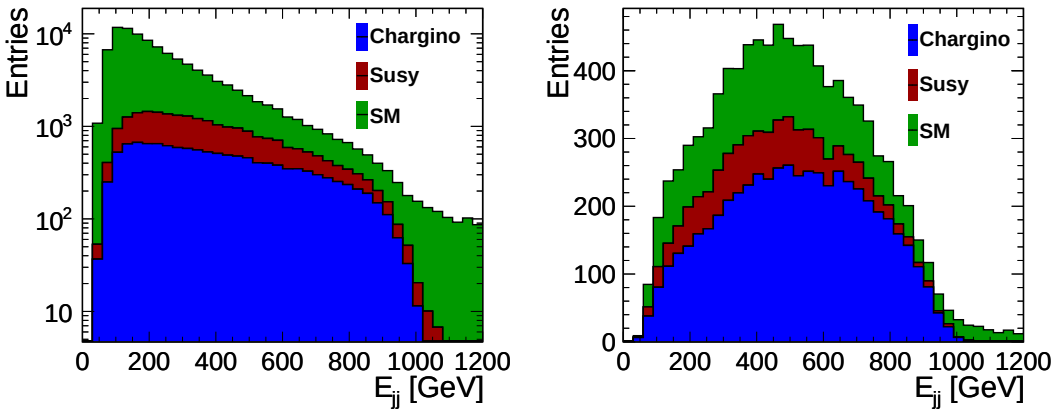

Figure 7: Reconstructed $W^{\pm}$ energy before (left) and after (right) the application of the BDT cut for the chargino signal and for the SM and SUSY backgrounds. The histograms are stacked on top of each other. All distributions are scaled to an integrated luminosity of 2 ab^{-1}.

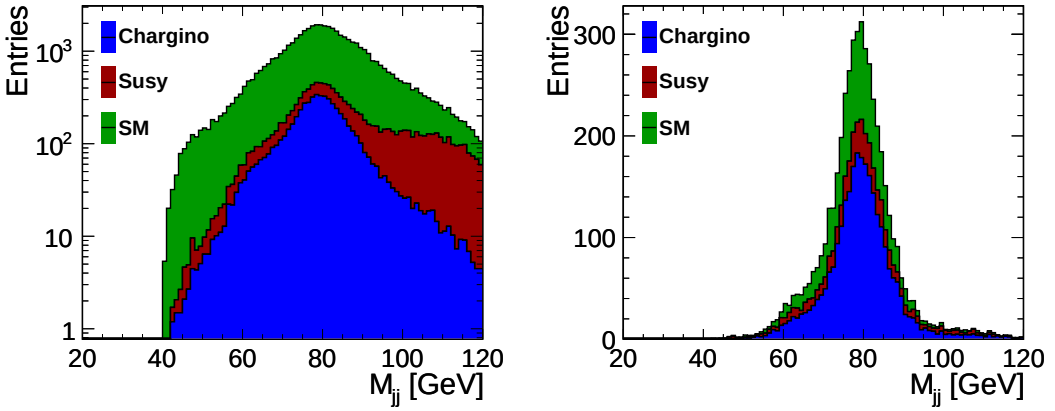

Figure 8: Reconstructed $W^{\pm}$ mass before (left) and after (right) the application of the BDT cut for the chargino signal and for the SM and SUSY backgrounds. The histograms are stacked on top of each other. All distributions are scaled to an integrated luminosity of 2 ab^{-1}.

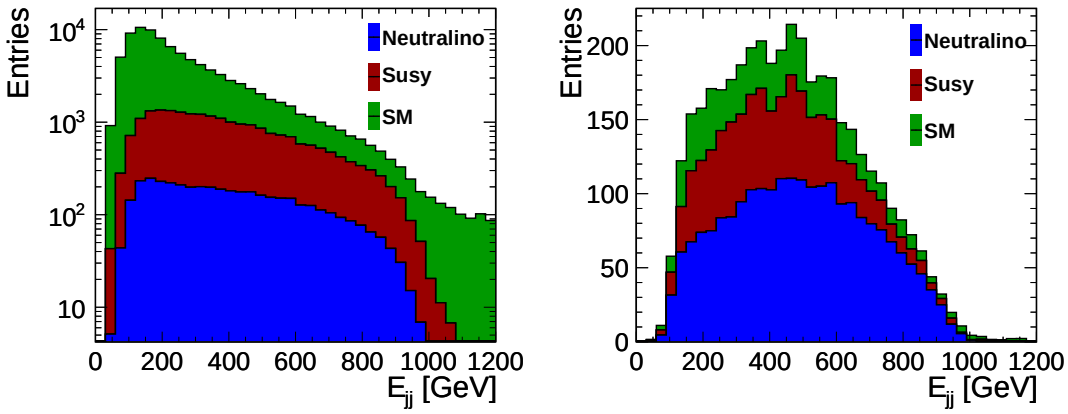

Figure 9: Reconstructed Higgs energy before (left) and after (right) the application of the BDT cut for the neutralino signal and for the SM and SUSY backgrounds. The histograms are stacked on top of each other. All distributions are scaled to an integrated luminosity of 2 ab^{-1}.

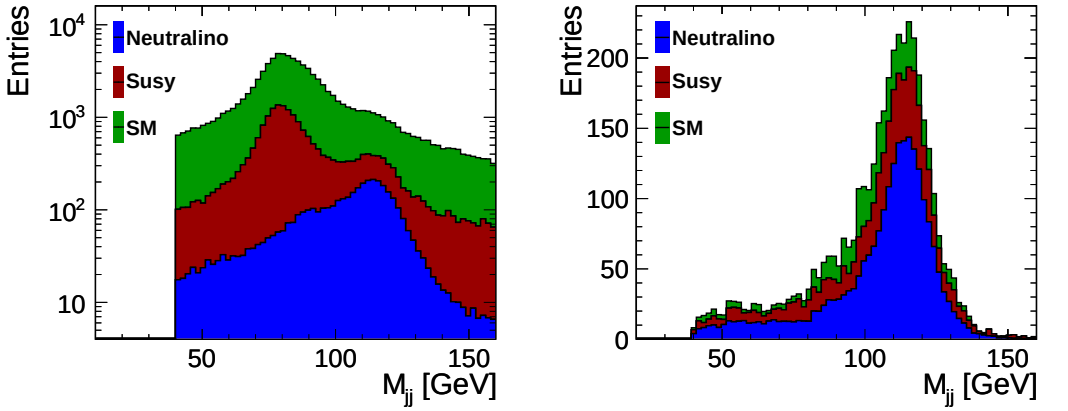

Figure 10: Reconstructed Higgs mass before (left) and after (right) the application of the BDT cut for the neutralino signal and for the SM and SUSY backgrounds. The histograms are stacked on top of each other. All distributions are scaled to an integrated luminosity of 2 ab^{-1}.

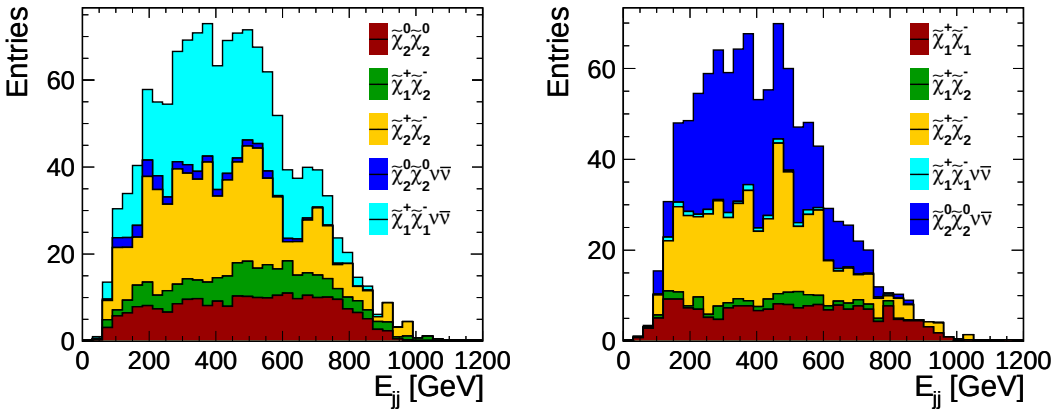

Figure 11: Composition of the SUSY background passing the chargino (left) and neutralino (right) selections. All contributions are scaled to an integrated luminosity of 2 ab^{-1}.

5. Signal extraction

Two complementary methods were used to extract masses and cross sections from the energy distributions of the reconstructed and selected $W^{\pm}$ and Higgs candidates (see Figs. 7 and 9). Both approaches are described in the following subsections.

5.1. Template fit

Cross sections and masses of the investigated SUSY particles were determined using the template method where signal Monte Carlo samples for different mass hypotheses were produced with full simulation and considering pileup from $\gamma\gamma \to$ hadrons. The masses were varied separately keeping the masses of all other SUSY particles at their default values. To avoid large uncertainties due to the limited statistics of the available Monte Carlo samples for some of the background processes, the sum of all backgrounds was parametrised using smooth functions. The obtained functions are compared to the sum of all background contributions for an integrated luminosity of 2 ab^{-1} in Fig. 12.

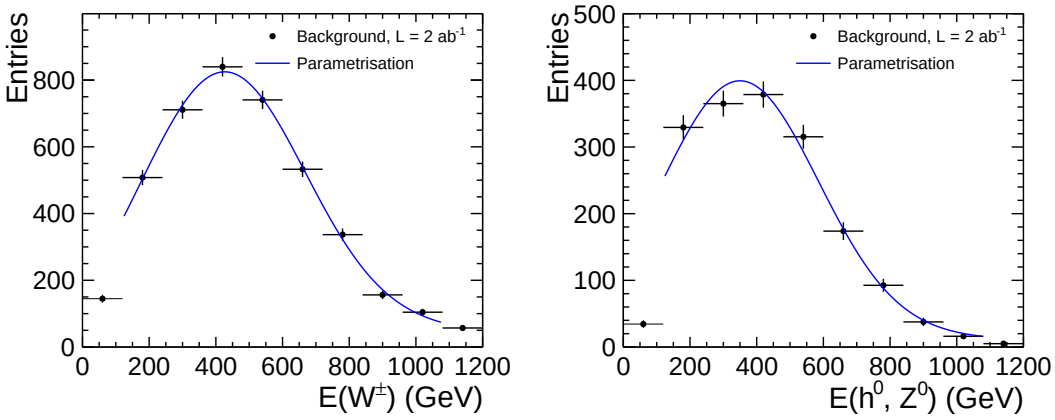

Figure 12: Parametrisation of the background for the chargino (left) and neutralino (right) data sets.

The fits were restricted to the energy range $120 < E(W^{\pm},h^0,Z^0) < 1080$ GeV to exclude bins with low statistics or regions where the parametrisation does not describe the backgrounds well. Apart from the masses and pair production cross sections of the $\tilde{\chi}_1^{\pm}$ or $\tilde{\chi}_2^0$ particles, the $\tilde{\chi}_1^0$ mass was extracted. This is possible, because the energy distribution of $W^{\pm}$ bosons from $\tilde{\chi}_1^{\pm}$ decays is sensitive to $M(\tilde{\chi}_1^0)$. Two-dimensional fits were performed simultaneously to the mass and production cross section for a given particle to account for the correlation between both quantities. The following function was minimised:

$$\chi_j^2 = \sum_{i=1}^{N} \frac{\left(n_{\text{data},i} - c_j \cdot n_{\text{template}_j,i} - n_{\text{background},i}\right)^2}{\sigma_{\text{data},i}^2 + \sigma_{\text{template}_j,i}^2}, \tag{4}$$

where the sum runs over all boson energy bins i. The optimal normalisation c_j was obtained for every tested mass value j. The number of entries in a given energy bin for the templates and for the measured distribution are referred to as $n_{\text{template}_j,i}$ and $n_{\text{data},i}$, respectively, while the corresponding statistical uncertainties are given by $\sigma_{\text{template}_j,i}$ and $\sigma_{\text{data},i}$. The expected number of background events is referred to as $n_{\text{background},i}$. The obtained minimal χ^2 values for different mass values are shown in Fig. 14.

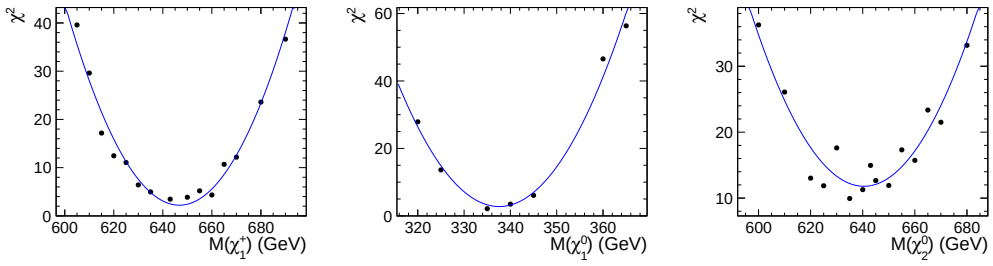

Figure 13: Minimal χ^2 values as a function of $M(\tilde{\chi}_1^{\pm})$ (left) and $M(\tilde{\chi}_1^0)$ (middle) from the chargino analysis, and $M(\tilde{\chi}_2^0)$ (right) from the neutralino analysis.

The optimal values of the SUSY particle masses were obtained from the minima of parabolas fitted to the χ^2 distributions. The toy MC method was used to estimate the statistical uncertainties of the measured masses. For this purpose, the data points in the measured boson energy distributions were smeared using a Gaussian distribution of width $\sqrt{n_{\text{data},i}}$, where $n_{\text{data},i}$ is the number of entries in a given bin. This step was repeated 5000 times and the optimal mass values are extracted for each iteration. The resulting distributions of optimal mass values is shown in Fig. 14. The widths of these distributions taken from fits of Gaussian peaks represent the statistical uncertainties of the measured chargino and neutralino masses.

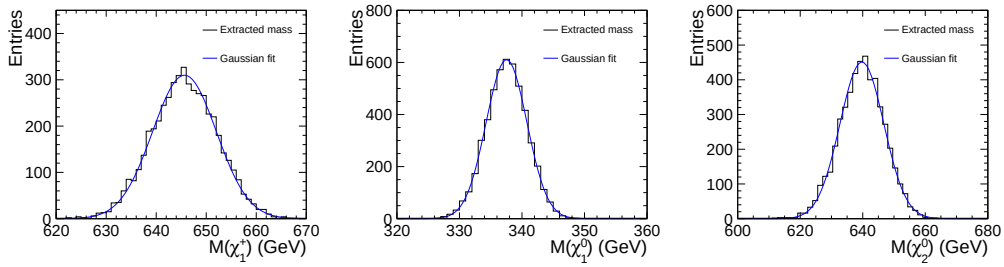

Figure 14: Distributions of $M(\tilde{\chi}_1^{\pm})$ (left) and $M(\tilde{\chi}_1^0)$ (middle) from the chargino analysis, and $M(\tilde{\chi}_2^0)$ (right) from the neutralino analysis obtained using a toy MC with 5000 iterations. The histograms were fitted using Gaussian distributions.

The cross sections and their statistical uncertainties were obtained in the same way. The

results are given in Tab. 2. Additionally, the fit results obtained when the number of bins in the reconstructed boson energy distributions was increased by a factor two are given in Tab. 3. The results demonstrate the stability of the fit procedure. All measured mass and cross section values are in agreement with the input values.

Parameter 1	Uncertainty	Parameter 2	Uncertainty
$M(\tilde{\chi}_1^{\pm})$	6.3 GeV	$\sigma(\tilde{\chi}_1^+\tilde{\chi}_1^-)$	2.2%
$M(\tilde{\chi}_1^0)$	3.0 GeV	$\sigma(\tilde{\chi}_1^+\tilde{\chi}_1^-)$	1.8%
$M(\tilde{\chi}_2^0)$	7.3 GeV	$\sigma(\tilde{\chi}_2^0\tilde{\chi}_2^0)$	2.9%

Table 2: Statistical uncertainties of the chargino and neutralino masses and pair production cross sections obtained from two parameter template fits. An integrated luminosity of 2 ab^{-1} is assumed.

Parameter 1	Uncertainty	Parameter 2	Uncertainty
$M(\tilde{\chi}_1^{\pm})$	6.2 GeV	$\sigma(\tilde{\chi}_1^+\tilde{\chi}_1^-)$	2.2%
$M(\tilde{\chi}_1^0)$	2.7 GeV	$\sigma(\tilde{\chi}_1^+\tilde{\chi}_1^-)$	1.8%
$M(\tilde{\chi}_2^0)$	7.2 GeV	$\sigma(\tilde{\chi}_2^0\tilde{\chi}_2^0)$	2.9%

Table 3: Same as Tab. 2, but the number of bins between 0 and 1200 GeV used for the histograms of the reconstructed boson energy distributions in the fit was increased from 10 to 20.

5.2. Least squares method

Linear least squares fits of gaugino masses and cross sections were used to check the results of the template fitting technique and to fit for three or more parameters simultaneously. Each $W^{\pm}/Z^0/h^0$ reconstructed energy histogram bin was expanded linearly about the nominal masses and cross sections. The slopes were obtained by convoluting a map of true-to-reconstructed bin contents with the true energy distributions at different gaugino masses, as detailed in Appendix B. No fits were actually performed; instead the bin statistical errors were calculated and then propagated to the fit parameter errors using standard formulae for linear least squares fits.

The least squares results for two parameter fits of one gaugino mass and one cross section are summarised in Tab. 4. These are to be directly compared with the template fit results of Tab. 2. Reasonable agreement is obtained for the two techniques.

The two parameter fits assume that the other SUSY parameters have been measured with arbitrary accuracy. Such an assumption can be relaxed one parameter at a time. For example, the $\tilde{\chi}_1^0$ mass will be measured with an accuracy of $\Delta M(\tilde{\chi}_1^0) = 3$ GeV at CLIC by combining the results from the slepton analyses [16]. A term constraining the $\tilde{\chi}_1^0$ mass to be within 3 GeV of the best estimate can be added to a three parameter least squares fit of $M(\tilde{\chi}_1^{\pm}), M(\tilde{\chi}_1^0), \sigma(\tilde{\chi}_1^+\tilde{\chi}_1^-)$ or $M(\tilde{\chi}_2^0), M(\tilde{\chi}_1^0), \sigma(\tilde{\chi}_2^0\tilde{\chi}_2^0)$. The results for such three parameter fits are shown in Tab. 5. The statistical uncertainties are somewhat larger compared to the two paramter fits.

Par. 1	Error	Par. 2	Error	$\rho(1,2)$
$M(\tilde{\chi}_1^{\pm})$	5.7 GeV	$\sigma(\tilde{\chi}_1^+\tilde{\chi}_1^-)$	2.0 %	0.51
$M(\tilde{\chi}_1^0)$	3.3 GeV	$\sigma(\tilde{\chi}_1^+\tilde{\chi}_1^-)$	1.8 %	0.23
$M(\tilde{\chi}_2^0)$	8.5 GeV	$\sigma(\tilde{\chi}_2^0\tilde{\chi}_2^0)$	3.0 %	0.40

Table 4: Statistical mass uncertainties, relative cross section uncertainties and correlation coefficients $\rho(1,2)$ from two parameter least squares fits. The reconstructed energy histograms contained 10 bins between 0 and 1200 GeV.

Par. 1	Error	Par. 2	Error	Par. 3	Error	$\rho(1,2)$	$\rho(1,3)$	$\rho(2,3)$
$M(\tilde{\chi}_1^{\pm})$	7.3 GeV	$M(\tilde{\chi}_1^0)$	2.9 GeV	$\sigma(\tilde{\chi}_1^+\tilde{\chi}_1^-)$	2.4 %	0.64	0.66	0.51
$M(\tilde{\chi}_2^0)$	9.9 GeV	$M(\tilde{\chi}_1^0)$	3.0 GeV	$\sigma(\tilde{\chi}_2^0\tilde{\chi}_2^0)$	3.2 %	0.52	0.49	0.33

Table 5: Statistical mass uncertainties, relative cross section uncertainties and correlation coefficients $\rho(i,j)$ from three parameter least squares fits which include the constraint that the $\tilde{\chi}_1^0$ mass be within 3 GeV of the value measured from slepton analyses. The reconstructed energy histograms contained 10 bins between 0 and 1200 GeV.

Finally one can combine the data from the $\tilde{\chi}_1^{\pm}$ and $\tilde{\chi}_2^0$ analyses and perform a five parameter least squares fit of $M(\tilde{\chi}_1^{\pm}), M(\tilde{\chi}_2^0), M(\tilde{\chi}_1^0), \sigma(\tilde{\chi}_1^+\tilde{\chi}_1^-), \sigma(\tilde{\chi}_2^0\tilde{\chi}_2^0)$. Again, we add the constraint that the $\tilde{\chi}_1^0$ mass be within 3 GeV of the value measured from slepton analyses. The results for this fit are shown in Tab. 6. The precisions obtained from the five parameter fit are very similar to those of the three parameter fits.

Parameter	Error
$M(\tilde{\chi}_1^{\pm})$	7.3 GeV
$M(\tilde{\chi}_1^0)$	2.9 GeV
$M(\tilde{\chi}_2^0)$	9.8 GeV
$\sigma(\tilde{\chi}_1^+\tilde{\chi}_1^-)$	2.4%
$\sigma(\tilde{\chi}_2^0\tilde{\chi}_2^0)$	3.2%

Table 6: Mass errors and relative cross section errors for a five parameter least squares fit which includes the constraint that the $\tilde{\chi}_1^0$ mass be within 3 GeV of the value measured from slepton analyses. The reconstructed energy histograms from both the $\tilde{\chi}_1^{\pm}$ and $\tilde{\chi}_2^0$ analyses are used where each histogram contains 10 bins between 0 and 1200 GeV.

6. Systematic uncertainties

The measurements described in this document are sensitive to the luminosity spectrum. To illustrate the effect of the uncertainty of the luminosity spectrum measurement, two variants of the luminosity spectrum were created "ad-hoc", in an attempt to mimic a change in beam conditions at the IP. In the first variant, for each beam 5% of the events were removed from the high energy peaks of the distributions and randomly distributed in the tails. As a second variation, the same number of events were moved from the tails of the distributions to the peaks. This corresponds to a change of the average $\sqrt{s'}$ by $\pm 1 \cdot 10^{-2}$. In both cases, the integral of the luminosity spectrum was not changed by this procedure.

The template fits were repeated with these distorted luminosity spectra used for the measured signal events while the templates were kept unchanged. This procedure simulates the effect of a very limited understandung of the luminosity spectum in measured data. The changes in the measured masses and cross sections, extracted using the distorted spectra, were compared to the values for the nominal spectra.

The variation described above translates to a change of the measured chargino and neutralino pair production cross sections that is similar in size as the statistical uncertainty. For the measured masses the variation of the luminosity spectrum leads to a shift that is typically half of the statistical uncertainty.

As an additional test, the normalisation of the SM background assumed in the template fits is changed by $\pm 15\%$ to evaluate the effect of the uncertainty of the Monte Carlo predictions. The impact on the fit results is found to be negligible.

7. Impact of beam polarisation

In this section, the impact of beam polarisation on the gaugino mass and pair production cross section measurements is discussed. For this purpose, two scenarios were investigated:

- $\pm 80\%$ polarisation for the electron beam and an unpolarised positron beam
- $\pm 80\%$ polarisation for the electron beam and $\pm 30\%$ polarisation for the positron beam

The first scenario corresponds to the baseline design of the CLIC machine while the second scenario might be realised in an upgrade of the CLIC accelerator.

The results described in this section were obtained using the template fit as described in Sec. 5.1. Since the kinematic properties of the chargino and neutralino candidates are not affected by polarisation for the signal samples as well as for the backgrounds, no additional samples were generated. However, the cross sections are strongly dependent on the beam polarisations. Hence the existing Monte Carlo samples summarised in Tab. 1 were reweighted for different beam polarisations. The template fits were repeated accordingly using the reweighted Monte Carlo samples.

All possible combinations of beam polarisations were tested for both scenarios. The best statistical precision was obtained for -80% electron polarisation for the first scenario and for -80% electron polarisation combined with +30% positron polarisation for the second scenario.

The statistical gaugino mass precision as a function of the integrated luminosity is shown in Fig 15 for these cases.

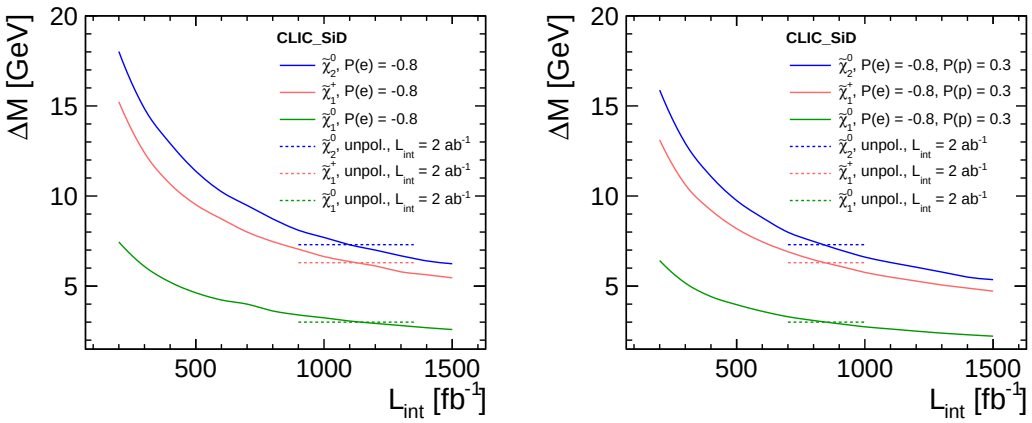

Figure 15: Statistical gaugino mass precision as a function of the integrated luminosity for -80% electron polarisation only (left) and for -80% electron polarisation combined with +30% positron polarisation (right). The horizontal lines represent the achieved mass precision with no polarisation assuming 2 ab^{-1} of integrated luminosity.

For an integrated luminosity of 1.12 ab^{-1} and an electron polarisation of -80% the same mass uncertainties were obtained as for 2 ab^{-1} of unpolarised data. In case of -80% electron polarisation combined with +30% positron polarisation an integrated luminosity of 0.84 ab^{-1} is required to achieve the same precision as for 2 ab^{-1} of unpolarised data.

The gaugino mass measurements are only weakly affected by the uncertainties of the beam polarisations. The effect of the beam polarisation uncertainties on the statistical precisions of the pair production cross sections is illustrated in Fig. 16. An uncertainty of the electron beam polarisation of up to 2% is uncritical for the pair production cross sections measurements in the first scenario, while a good knowledge of the positron polarisation is crucial in the second scenario.

8. Conclusion and Summary

The signals from $\tilde{\chi}_1^{\pm}$ and $\tilde{\chi}_2^0$ pair production are extracted from fully hadronic final states with four jets and missing transverse energy. The study was performed using full simulation and considering pileup from $\gamma\gamma \to$ hadrons. Two different signal extraction procedures are in reasonable agreement. The chargino and neutralino pair production cross sections are extracted with a statistical precision of $2-3\%$ while the masses of the $\tilde{\chi}_1^{\pm}$, $\tilde{\chi}_1^0$ and $\tilde{\chi}_2^0$ particles are determined with typical statistical accuracies of about $1-1.5\%$. Beam polarisation allows to obtain the same precisions using significantly smaller data samples.

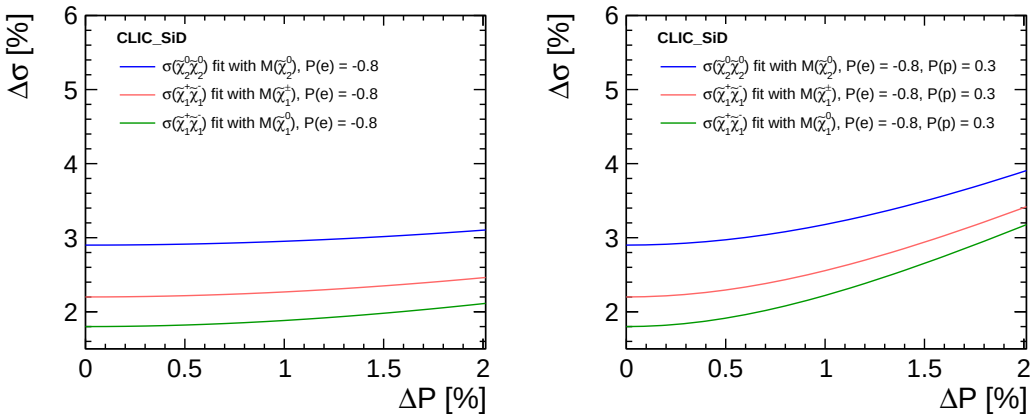

Figure 16: Statistical precisions of the gaugino pair production cross sections as functions of the polarisation uncertainty for -80% electron polarisation only (left) and for -80% electron polarisation combined with +30% positron polarisation (right). The left plot assumes an integrated luminosity of 1.12 ab^{-1} while the right plots assumes an integrated luminosity of 0.84 ab^{-1}, as motivated by the discussion in the text.

A. Purities and efficiencies as functions of the $W^{\pm}$ and Higgs energies

The purity and efficiency of the chargino selection are shown as a function of the $W^{\pm}$ candidate energy for different choices of the BDT cut in Fig. 17. The efficiency is lower at lower values of the $W^{\pm}$ energy.

The purity and efficiency of the neutalino selection are shown as a function of the Higgs candidate energy for different BDT cut values in Fig. 18. Also for the neutralino signal the efficiency is lower at lower values of the Higgs energy.

B. Details on the least squares fit

Let $\rho(\vec{z},\vec{\theta})$ be the true distribution of observables $\vec{z}$ with $\vec{\theta}$ the parameters we wish to measure, such as the chargino and neutralino masses. We write $\vec{z} = (x_+, x_-, \vec{y})$ to indicate that the observables x_+ and x_- will be combined in a single histogram, and that we will integrate over the observables $\vec{y}$.

Let $b_i(\vec{\theta})$ and $c_i(\vec{\theta})$ be the true and measured content, respectively of bin i:

$$b_i(\vec{\theta}) = b_{+i}(\vec{\theta}) + b_{-i}(\vec{\theta}) \tag{5}$$

where

$$b_{+i}(\vec{\theta}) = \int_{x_i}^{x_{i+1}} dx_+ f_+(x_+,\vec{\theta}), \quad b_{-i}(\vec{\theta}) = \int_{x_i}^{x_{i+1}} dx_- f_-(x_-,\vec{\theta}) \tag{6}$$

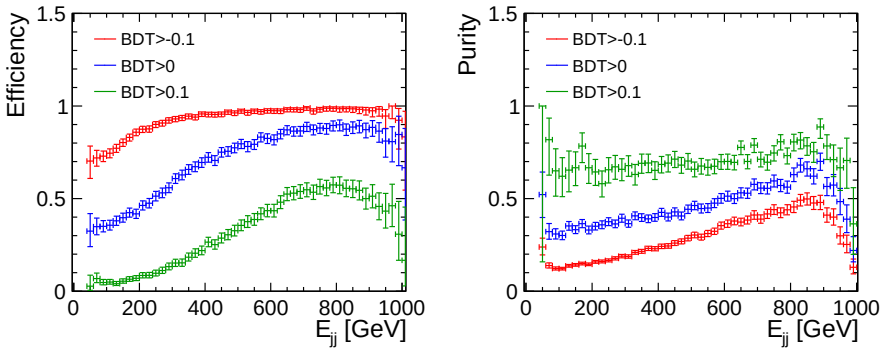

Figure 17: Efficiency (left) and purity (right) as function of the reconstructed $W^{\pm}$ candidate energy for different BDT cut values.

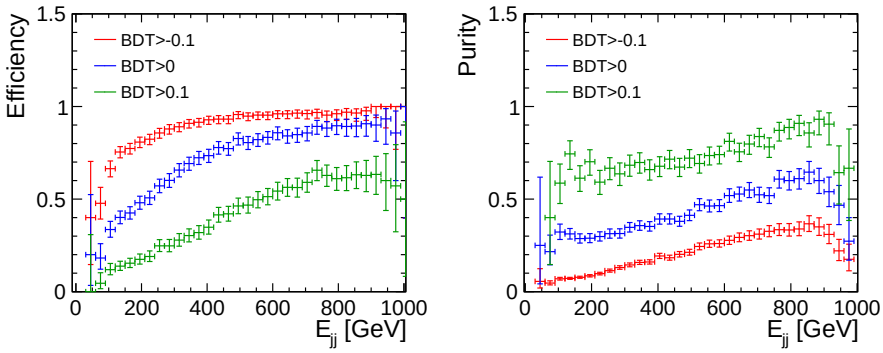

Figure 18: Efficiency (left) and purity (right) as function of the reconstructed Higgs candidate energy for different BDT cut values.

and

$$f_+(x_+,\vec{\theta}) = \int dx_-\, d\vec{y}\, \rho(x_+,x_-,\vec{y},\vec{\theta}), \quad f_-(x_-,\vec{\theta}) = \int dx_+\, d\vec{y}\, \rho(x_+,x_-,\vec{y},\vec{\theta}). \tag{7}$$

Let $\Omega(x'_+,x'_-,\vec{z})$ be the resolution function and $\eta(\vec{z})$ be the detection efficiency. If we define

$$\Omega_+(x'_+,\vec{z}) \equiv \int dx'_-\,\Omega(x'_+,x-',\vec{z}), \quad \Omega_-(x'_-,\vec{z}) \equiv \int dx'_+\,\Omega(x'_+,x'_-,\vec{z}) \tag{8}$$

then

$$c_i(\vec{\theta}) = \int_{x_i}^{x_{i+1}} dx'_+ \int d\vec{z}\,\Omega_+(x'_+,\vec{z})\eta(\vec{z})\rho(\vec{z},\vec{\theta}) + \int_{x_i}^{x_{i+1}} dx'_- \int d\vec{z}\,\Omega_-(x'_-,\vec{z})\eta(\vec{z})\rho(\vec{z},\vec{\theta})\,. \tag{9}$$

The measured bin content $c_i(\vec{\theta})$ can be rewritten as

$$c_i(\vec{\theta}) = \int_{x_i}^{x_{i+1}} dx'_+ \int dx_+ h_+(x'_+, x_+, \vec{\theta}) f_+(x_+, \vec{\theta}) + \int_{x_i}^{x_{i+1}} dx'_- \int dx_- h_-(x'_-, x_-, \vec{\theta}) f_-(x_-, \vec{\theta}) \tag{10}$$

where

$$h_+(x'_+, x_+, \vec{\theta}) \equiv \int dx_- d\vec{y}\, \Omega_+(x'_+, \vec{z}) \eta(\vec{z}) \frac{\rho(\vec{z}, \vec{\theta})}{f_+(x_+, \vec{\theta})} \ . \tag{11}$$

and the function $h_-(x'_-, x_-, \vec{\theta})$ is defined similarly.

If the fit parameters $\vec{\theta}$ are expanded about their pre-fit best estimates $\vec{\theta}_0$,

$$\vec{\theta} \approx \vec{\theta}_0 + \Delta\vec{\theta} \ , \tag{12}$$

then the function $h_+(x'_+, x_+, \vec{\theta})$ can be written as

$$h_+ \approx \int dx_- d\vec{y}\, \Omega_+(x'_+, \vec{z}) \eta(\vec{z}) \frac{\rho(\vec{z}, \vec{\theta}_0)}{f_+(x_+, \vec{\theta}_0)} \left[1 + \Delta\vec{\theta} \bullet \left(\frac{1}{\rho(\vec{z}, \vec{\theta}_0)} \frac{d\rho}{d\vec{\theta}} - \frac{1}{f_+(x_+, \vec{\theta}_0)} \frac{df_+}{d\vec{\theta}} \right) \right] \ . \tag{13}$$

If, as is the case in the least squares fits being studied here,

$$\left| \Delta\vec{\theta} \bullet \left(\frac{1}{\rho(\vec{z}, \vec{\theta}_0)} \frac{d\rho}{d\vec{\theta}} - \frac{1}{f_+(x_+, \vec{\theta}_0)} \frac{df_+}{d\vec{\theta}} \right) \right| << 1 \tag{14}$$

then h_+ and h_- are independent of θ and

$$\begin{aligned} c_i(\vec{\theta}) &= \int_{x_i}^{x_{i+1}} dx'_+ \int dx_+ h_+(x'_+, x_+) f_+(x_+, \vec{\theta}) + \int_{x_i}^{x_{i+1}} dx'_- \int dx_- h_-(x'_-, x_-) f_-(x_-, \vec{\theta}) \\ &\approx \sum_j \int_{x_i}^{x_{i+1}} dx'_+ h_+(x'_+, x_j) \int_{x_j}^{x_{j+1}} dx_+ f_+(x_+, \vec{\theta}) + \int_{x_i}^{x_{i+1}} dx'_- h_-(x'_-, x_j) \int_{x_j}^{x_{j+1}} dx_- f_-(x_-, \vec{\theta}) \\ &= \sum_j \int_{x_i}^{x_{i+1}} dx'_+ h_+(x'_+, x_j) b_{+j}(\vec{\theta}) + \int_{x_i}^{x_{i+1}} dx'_- h_-(x'_-, x_j) b_{-j}(\vec{\theta}) \\ &\approx \sum_j H_{ij} b_j(\vec{\theta}) \ \text{ where } H_{ij} = (x_{i+1} - x_i) h_+(x_i, x_j) = (x_{i+1} - x_i) h_-(x_i, x_j) \end{aligned} \tag{15}$$

H_{ij} is the matrix that maps the true to reconstructed bin contents.

References

[1] L. Linssen (Ed.) et al., *Physics and Detectors at CLIC - CLIC Conceptual Design Report*, CERN-2012-003 (2012).

[2] M. Thomson et al., *The physics benchmark processes for the detector performance studies of the CILC CDR*, LCD-Note-2011-016 (2011).

[3] W. Kilian, T. Ohl and J. Reuter, *WHIZARD: Simulating Multi-Particle Processes at LHC and ILC*, arXiv:0708.4233 (2007);
M. Moretti et al., *O'Mega: An Optimizing Matrix Element Generator*, LC-TOOL-2001-040, also arXiv:hep-ph/0102195 (2001).

[4] M. Skrzypek and S. Jadach, *Exact and approximate solutions for the electron nonsinglet structure function in QED*, Z. Phys. C 49 (1991) 577.

[5] B. Dalena, J. Esberg and D. Schulte, *Beam-induced backgrounds in the CLIC 3 TeV CM energy interaction region*, Proceedings of LCWS11, arXiv:1202.0563 (2012).

[6] T. Sjörstrand, S. Mrenna and P. Skands, *PYTHIA 6.4 physics and manual* , JHEP 05 (2006) 026.

[7] C. Grefe and A. Münnich, *The CLIC_SiD_CDR Detector Model for the CLIC CDR Monte Carlo Mass Production*, LCD-Note-2011-009 (2011).

[8] Simulator for the Linear Collider (SLIC), `http://www.lcsim.org/software/slic/`.

[9] S. Agostinelli et al., *GEANT4 - a simulation toolkit*, Nucl. Instr. Meth. A 506 (2003) 250;
J. Allison et al., *Geant4 Developments and Applications*, IEEE Trans. Nucl. Sci. 53 (2006) 270.

[10] C. Grefe, *OverlayDriver - an Event Mixing Tool for org.lcsim*, LCD-Note-2011-032 (2011).

[11] J. Marshall and M.A. Thomson, *Redesign of the Pandora Particle Flow algorithm*, Report at IWLC2010 (2010).

[12] M.A. Thomson, *Particle Flow Calorimetry and the PandoraPFA Algorithm*, Nucl. Inst. Meth. A 611 (2009) 25.

[13] S. Catani et al., *Longitudinally-invariant $k_\perp$-clustering algorithms for hadron-hadron collisions*, Nucl. Phys. B 406 (1993) 187;
S.D. Ellis and D.E. Soper, *Successive combination jet algorithm for hadron collisions*, Phys. Rev. D 48 (1993) 3160.

[14] M. Cacciari, G.P. Salam, *Dispelling the N^3 myth for the k_t jet-finder*, Phys. Lett. B 641 (2006) 57;
M. Cacciari, G.P. Salam and G. Soyez, `http://fastjet.fr/`.

[15] A. Hoecker et al., *TMVA 4 - Toolkit for Multivariate Data Analysis with ROOT*, arXiv:physics/0703039, also CERN-OPEN-2007-007 (2009).

[16] M. Battaglia et al., *Physics performances for Scalar Electrons, Scalar Muons and Scalar Neutrino searches at CLIC*, LCD-Note-2011-018 (2011).